The effect of sputtering oblique angle on large area deposition: a unidirectional ultrathin gold film growth design

Hicham Bakkali, Eduardo Blanco, M. Dominguez, Maria Beatriz de La Mora, Citlali Sánchez-Aké, Mayo Villagrán-Muniz, D. S. Schmool, Bruno Berini, S. E. Lofland

The effect of sputtering oblique angle on large area deposition: a unidirectional ultrathin gold film growth design

H.Bakkali[1], E.Blanco[1], M.Dominguez[1], M.B.de la Mora[2], C.Sánchez-Aké[3], M.Villagrán-Muniz[3], D. S. Schmool[4], B. Berini[4] and S. E. Lofland [5]

[1]Departamento de Física de la Materia Condensada and IMEYMAT: Institute of Research on Electron Microscopy and Materials, University of Cadiz, E11510 Puerto Real, Cádiz, Spain

[2]CONACyT Research Fellow-ICAT, Universidad Nacional Autónoma de México (UNAM), México, D.F. 04510, México

[3]Instituto de Ciencias Aplicadas y Tecnología (ICAT), Universidad Nacional Autónoma de México (UNAM), México, D.F. 04510, México

[4]Groupe d'Etude de la Matière Condensée GEMaC, CNRS (UMR 8635), Université de Versailles/Saint-Quentin-en-Yvelines, Université Paris-Saclay, 45 Avenue des États-Unis, 78035, Versailles, France

[5]Department of Physics and Astronomy, Rowan University, 201 Mullica Hill Road, Glassboro, NJ 08028, USA

Abstract

Growing ultrathin nanogranular (NG) metallic films with continuously varying thickness is of great interest for studying regions of criticality and scaling behavior in the vicinity of quantum phase transitions. In the present work, an ultrathin gold NG film was grown on a sapphire substrate by RF magnetron sputtering at an oblique angle of 60º to produce a gradient in the film thickness with a nominal thickness *t* ranging from 5 to 13 nm. The nanostructural properties were examined with high-resolution transmission electron microscopy, X-ray diffraction and reflectivity techniques The film growth can be described in terms of the Volmer-Weber (VW) mode. The optical and electronic transport measurements indicated a clear phase transition in the electronic transport from a quantum tunnelling regime to a metallic conduction one when *t* exceeds a critical value of ~ 7.8 nm. We demonstrate that by using a

continuously varying thickness we can unambiguously identify the criteria for metallicity.

1. Introduction

During the last few decades, nanomaterials have led the way in the discovery of new phenomena and the exploration of new models and theories in material science and modern condensed matter physics [1,2]. Nanomaterials present many opportunities for great impact on both basic research and technological applications. For instance, nanogranular (NG) metal thin films consisting of metal nanoparticles (NPs) randomly distributed in an insulating matrix, have received considerable attention due to their potential applications in electronic, electromagnetic, plasmonic and microwave devices [3–5]. For fundamental research, they are of great interest for studying quantum interactions, electronic correlation effects, and inter-particle electromagnetic coupling, among others [6–8]. The control of their structure through synthesis and subsequent processing plays an important role in tailoring their final properties since their electrical, magnetic and optical response can be tuned by varying a few physically significant parameters such as the size, composition, distribution and shape of the NPs as well as the type of the surrounding medium [5].

Physical vapor deposition (PVD) processes such as radiofrequency (RF) and direct current (DC) magnetron sputtering, as well as pulsed laser and electron beam deposition techniques are commonly used for producing high quality NG metallic thin films and coatings. Their usage can be attributed to their reproducibility, relatively low cost, and environmentally friendly characteristics. In the last twenty years, oblique angle deposition has received particular attention because of its singular ability to obtain highly ordered nanoscale inclusions on the film surface with a range of anisotropy and porosity [9–11]. Krause [12] pointed out that the porosity is only apparent at a certain deposition angle above 60º. This process has yielded interesting microstructures such as

helical nano-columnar, tilted and uniformly aligned nanorod arrays [13] that can be potentially applied as antireflective coatings and optical filters.

To date, most of the studies reported in the literature on the quantum phase transition of electrical conductivity in NG metals were carried out with samples of discrete thicknesses [14–18]. The difficulty with such studies is that the difference between consecutive values in the studied range may be too large, omitting important transition regions, especially when the behavior displays critical scaling behavior. Specifically, questions regarding the exact crossover of the static dielectric constant ε_1 from negative to positive occurs [ref. first paper?] and the transition from localized surface plasmon resonance (LSPR) to surface plasmon-polariton resonance (SPPR) in metallic NPs evolve to a continuous metal have not been addressed. Here we investigate the microstructural and optical properties of a film of gold NPs with a gradient in thickness to systematically answer these questions.

2. Experimental

A gold NG thin film was deposited by sputtering from Au target onto a single-side polished (SPP) sapphire wafer (50 mm diameter). Four equidistant gold foil squares with sizes of 5 × 5 mm^2 were located 12.5 mm away from the center of the TiO_2 target [19] which was 10 cm from the substrate. The sputtering gun was tilted by ~ 60° from the substrate normal in order to create a film with a thickness gradient across the sapphire substrate. The argon pressure was set at 36 mTorr (4.8 Pa), and a deposition power of 25 W with a deposition time of 20 min were used.

At different selected positions along the substrate, several carbon grids were situated for use in high-resolution transmission electron microscopy (HR-TEM) analysis performed with a JEOL 2010-HR-TEM. X-ray diffraction (XRD) and x-ray reflectivity

(XRR) measurements were carried out with a Panalytical Empyrean x-ray diffractometer with a two-bounce hybrid monochromator and Cu $K_{\alpha 1}$ radiation. XRD data were analyzed with Panalytical High Score Plus software while XRR data were fitted with the Panalytical Reflectivity program. Additionally, the film surface roughness was studied with a Bruker Dimension Icon atomic force microscope (AFM) with ScanAsyst and equipped with the Nanoscope software (Bruker Nanoscope V). The AFM topography measurements were performed in air with peak force tapping mode. For this purpose, a silicon tip on nitride lever (ScanAsyst Air model), with a 0.4 N/m spring constant and a nominal tip radius of 2 nm, was used to analyze regions of 0.5 × 0.5 μm^2 with a resolution of 256 pixels × 256 pixels.

For the studies of the optical properties, a Woollam VVASE vertical variable angle spectroscopic ellipsometer was employed in the ultraviolet-visible-near infrared (UV-Vis-NIR) region 300-1700 nm (5880-33333cm^{-1}) along the maximum thickness gradient direction with a 200-μm diameter spot size. Furthermore, we also measured the normal incidence UV-Vis-NIR transmittance *T* for an ultrathin gold NG film deposited on double side polished quartz wafer under nominally identical deposition conditions. In this case, different translation steps were employed in the spectral range of 250-2500 nm (along to the same direction of maximum thickness gradient), 0.3 mm for the first 100 measured spectra and 1 mm for the further 17 measured spectra, with a total of 117 spectra with a spot size of 400 μm. Finally, to study the electrical properties, *dc* resistivity ρ_{dc} was measured by the Van der Pauw method with a probe station equipped with a Jandel four-point probe with 0.625 mm spacing, and a Keithley current source.

2. Results and Discussion

The XRR data were analyzed with a three-layer model consisting of a core layer accompanied by thin porous top and bottom interfacial layers to account for the

roughness due to granularity (see Supporting Information). At the smallest angles, the x-ray beam irradiates a large area of the sample, and since the values for the density are sensitive to the features near the critical angle, those values may have substantially larger errors than those expected from the fit alone. However, the total thickness t is much more robust since the Kiessig oscillations occur at much higher angles.

The X-ray diffraction pattern showed only two peaks which were indexed to the Au fcc (111) and (222) reflections. XPS (Supplementary Information) indicated a small amount of Ti which likely led to amorphous TiO_x. The average nanocrystallite height D (Fig. 1a) was determined from Williamson-Hall plots to separate out the size and strain contributions to the linewidth, and the errors in D were estimated based upon the errors in determining the width. There is a linear relationship between D and t although it is not simply a proportional one – extrapolation of the line suggests that t disappears when D is non-zero. This reflects the difference in the two measurements. If the crystallites are small enough and not of enough density, then a film thickness is not detectable by XRR even though the individual NPs can be measured with XRD. Figure 1b shows the average film density ρ_{avg} estimated by combining the XRR and XRD data where $\rho_{avg} \propto I/t$ with I being the integrated XRD intensity.

Figure 2 shows the TEM results where the darker regions correspond to crystalline gold that shows lattice contrast due to the atomic planes. The sample exhibited a transition from isolated islands (Fig. 2a) towards worm-like networks (Fig. 2 b-d) as the NPs tended to increase in size, merge together to form nanoclusters and eventually coalesce. The AFM results likewise displayed a clear transition in the film texture from being granular (Fig. 3 a-g) to being continuous (Fig. 3 h-l). The surface roughness (Fig. 3 m) increases with the film thickness as the islands grew, reaching a maximum when the NPs merge near $t = 7$ nm and then decreases as the gaps are filled.

The microscopy studies allow one to more meaningfully interpret the x-ray data. As the islands grow, ρ_{avg} (Fig. 1b) increases until the grains merge at t = 7 nm where t and D coincide (Fig 1a). At larger thicknesses, new grains nucleate on top of the bottom grains and create some voids while covering the gaps so that the average grain size grows more slowly than the film thickness (Fig. 1a) and ρ_{avg} decreases due to the voids (Fig. 1b). These observations are consistent with Volmer-Weber growth [20,21], shown schematically in Fig. 4.

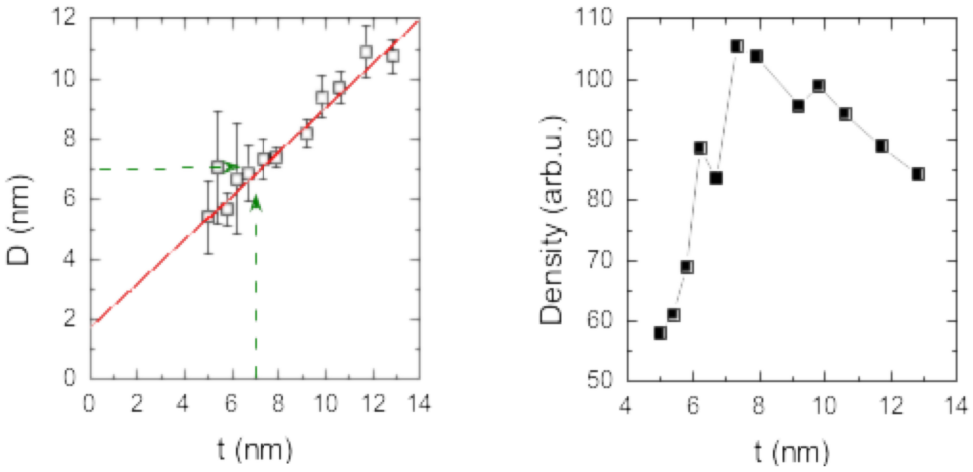

Figure 1. X-ray results. *(a) Dependence of nanocrystallite diameter determined by XRD as a function of the total film thickness determined from XRR. The solid line is a linear fit to the data. (b) The average density in arbitrary units, determined from XRR and XRD measurements. At around 7 nm, the particle diameter and the film thickness coincide, which is also where the average density is greatest.*

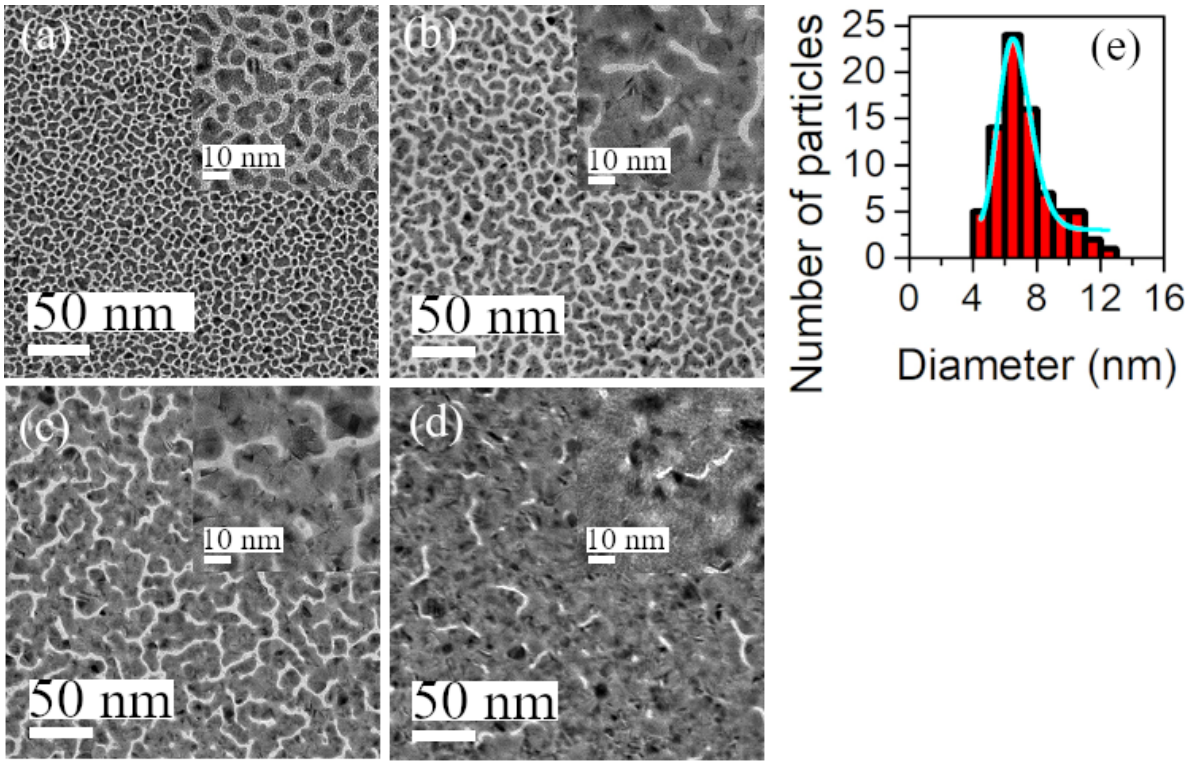

Figure 2. *TEM images of the Au NG thin films obtained at different values of t (a) 5 nm, (b) 7.5 nm, (c) 9.8 nm, and (d) 13 nm. The dark regions indicate the Au particles. (e) Histograms of the particle size distribution at t = 5 nm fitted with a log-normal distribution.*

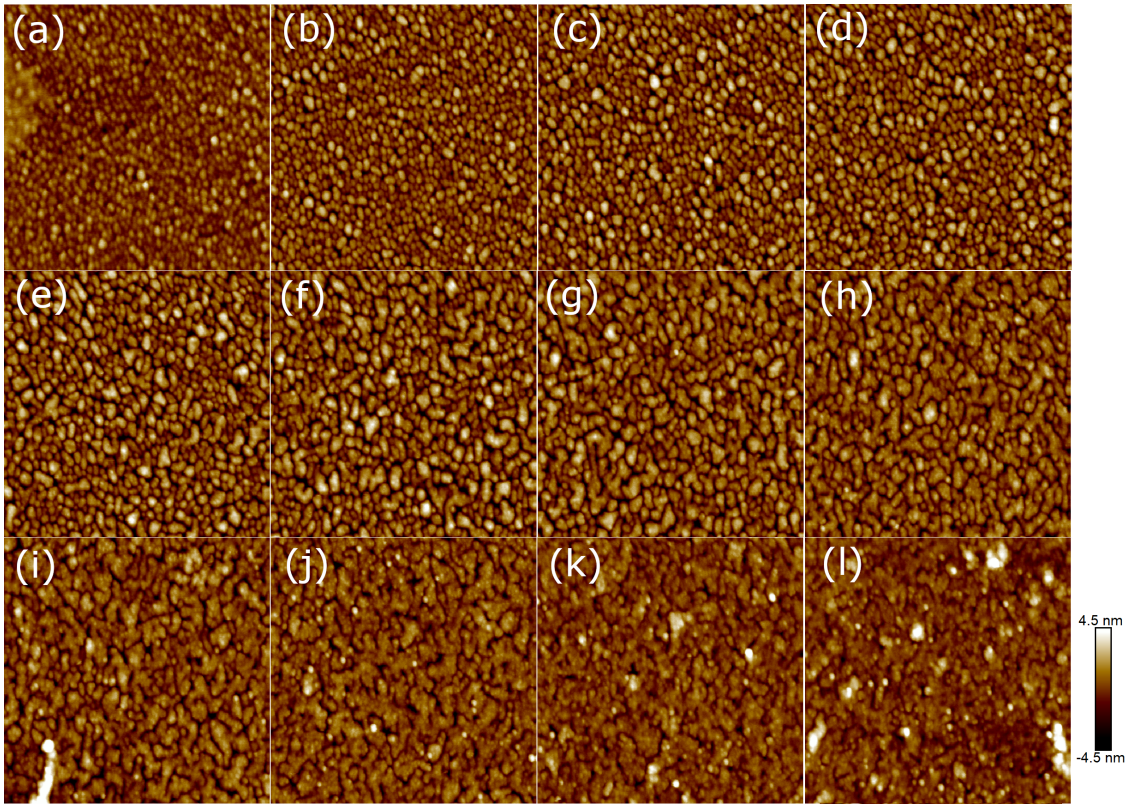

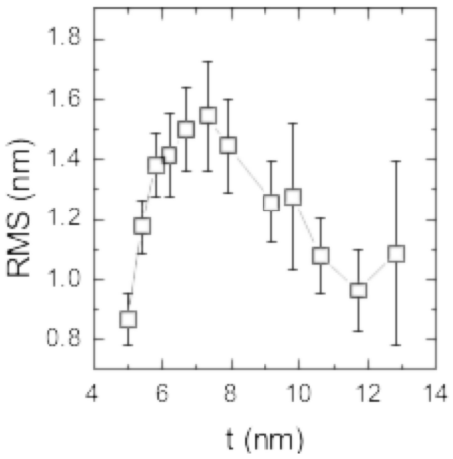

Fig. 3. *The representative topographic images obtained at different distances along the maximum thickness gradient direction. In all cases, a* 0.5 × 0.5 μm^2 *scan size area was analyzed at 4 mm translation step. Bottom: thickness dependence of the Root Mean Square (RMS)values obtained at different distances along the maximum thickness gradient direction.*

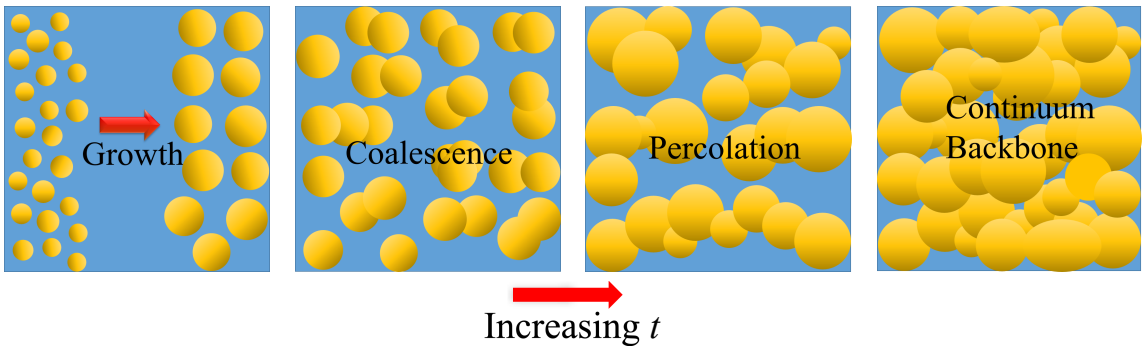

Fig. 4 *Sketch model of the Au-NG film stages of growth: growth of NPs, coalescence, percolation and the continuum backbone.*

The ellipsometric angle, amplitude ratio ψ, and phase difference Δ between the reflected parallel *p* and perpendicular *s* components were measured at an angle of incidence of 70º. They can be expressed as a function of the ratio between $\hat{R}_p$ and $\hat{R}_s$ which are the parallel and perpendicular Fresnel reflection coefficients as follows:

$$\hat{\rho} = \frac{\hat{R}_p}{\hat{R}_s} = \tan\psi e^{i\Delta} \tag{3}$$

Accordingly, Δ is more sensitive to small changes in film thickness than ψ since it measures the phase differences between the measured reflected *p* and *s* components rather than the amplitude $\frac{|\hat{R}_p|}{|\hat{R}_s|}$.

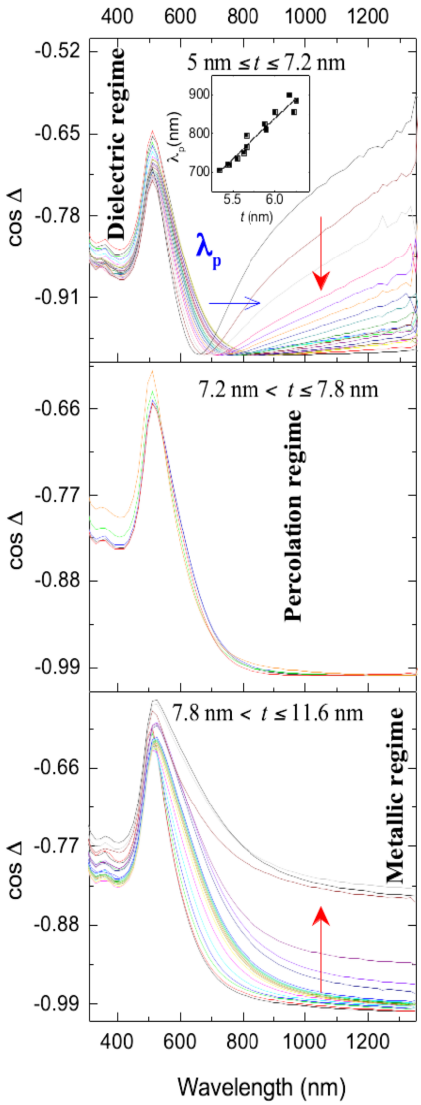

Figure 5. *Ellipsometry spectra:* cos *Δ measured at different t values plotted versus wavelength (λ).*

Figure 5 shows the experimental ellipsometry spectra, representing cos Δ as a function of wavelength λ. The spectra exhibit meaningful features depending on the film thickness ranges: when 5 nm ≤ *t* ≤ 7.2 nm, the spectra display some dips with a

characteristic wavelength λ_p in the Vis-NIR region (660-885 nm) which is associated with the LSPR for the Au NPs. These dips shift slightly towards longer wavelengths (red shift) with increasing t with a concomitant broadening. As shown in the inset of figure 5, λ_p linearly increases with t until the features disappear for $t > 7.2$ nm, the percolation onset [ref].

Another interesting point shown here is that the cos Δ spectra display significant wavelength dependence in the NIR region as a function of t: (i) a pronounced LSPR absorption increasing in the range 5 nm ≤ t ≤ 7.2 nm that could be attributed to a dielectric regime (region D) when most of the gold NPs are isolated, (ii) a very weak wavelength dependence, i.e., a plateau region, when 7.2 nm < t ≤ 7.8, which reveals the typical feature of the percolating network (region P) [24–26], (iii) the transition metal-like behavior occurs yielding to an absorption decrease when $t > 7.8$ nm (region M).

To accurately evaluate the effective optical constants, the incident angle independent pseudodielectric functions were fitted with a three-phase model (air/film/sapphire) including different combinations of Gaussian and Drude oscillators [19,27,28], accounting for the Au LSPR and the free-electron contribution to the electronic transport, respectively, from which the complex dielectric function was determined at each measured sample point.

$$\hat{\varepsilon}(\omega) = \varepsilon(\omega)_{Drude} + \sum_{n=1}^{N} \varepsilon_n(\omega)_{Gaussian} + \varepsilon_\infty \tag{4}$$

where $\varepsilon_{nGaussian} = \varepsilon_{n1} + i\varepsilon_{n2}$ is the n^{th} complex Gaussian oscillator function with ε_{n1} obeying the Kramers–Kronig relationship. A pure multi-Gaussian oscillator model, with three oscillators, was used in the dielectric region; two Gaussian and one Drude oscillator in the percolation region, and one Gaussian and one Drude oscillator in the

metallic region. In all cases, an additional 2 Gaussian oscillators were required to describe the Au *d* electron interband transitions in the UV region.

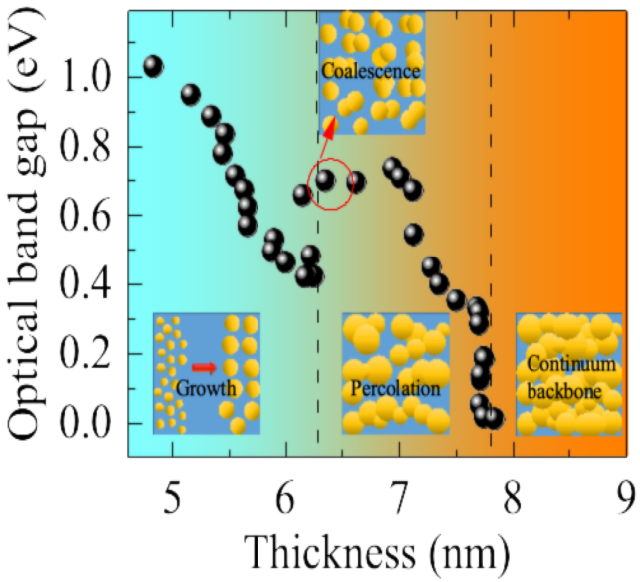

Figure 6. *Thickness dependence of the optical band gap.*

From the ellipsometric results, the absorption coefficient α spectrum was calculated for the studied thickness range. According to Tauc, the optical band gap of the film follows the expression [32]:

$$(\alpha h\nu) = c(h\nu - E_g)^2 \quad , \tag{6}$$

for an indirect allowed transition. Figure 6 shows the optical band gap obtained from the Tauc plots. In region (a), the optical gap drastically decreased from 1 eV to 0.4 eV with increasing *t* due to the reduction of the inter-particle distance as the band gap depends sensitively on the tunnel barrier thickness. However, it is interesting to note that the *t* dependence of the band gap shows a discontinuity at *t*= 6.3 nm which probably arises from the onset of coalescence. It remains constant with increasing thickness but then shows a precipitous drop near peroclation at *t* = 7.2 nm. At *t* = 7.8 nm, a second discontinuity is observed as the band gap disappears because of the transition to metal-

like behavior, as previously found from the zero crossover of the dielectric constant, ε_1 .

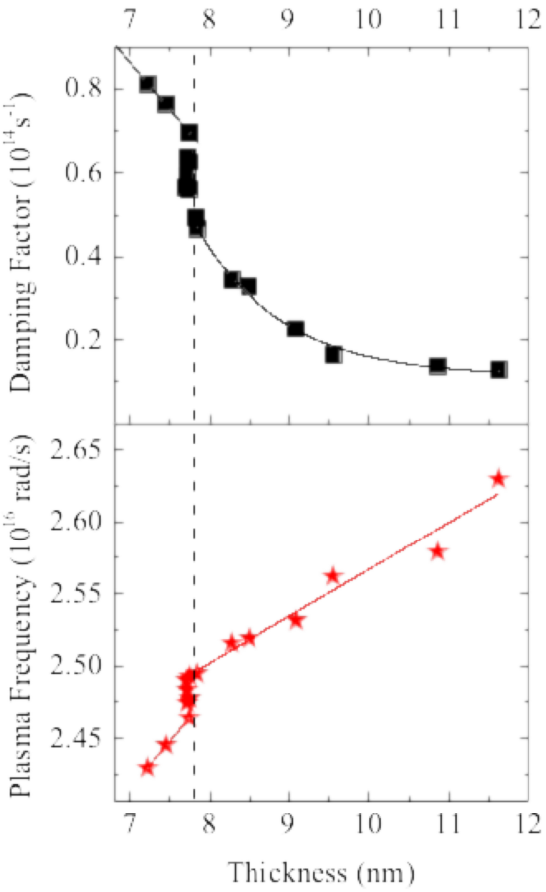

Figure 7. *Thickness dependence of the damping factor of the Drude oscillator and the plasma frequency. Solid lines are guides for the eye.*

The crossover to metallicity is also manifested in discontinuities in both the damping factor of the Drude oscillator and the plasma frequency (Figure 7). It is well known that when the film thickness is reduced to less than the average mean free path of the bulk material, surface and defect scattering effects are expected to be dominant [33]. Here, the largest value of t was significantly smaller than the typical value for the mean free path of gold ~ 42 nm. Consequently, an increase of t from ~ 7 nm to 13 nm resulted in a decreased Drude damping factor, as expected, since it should disappear as the thickness increases above the mean free path of the bulk material [33]. The plasma frequency, which depends on the carrier density, is found to increase with t due to the

competition between the free carriers and tunneling from isolated NPs in the percolating regime. The tunneling contribution disappears when the film becomes metallic.

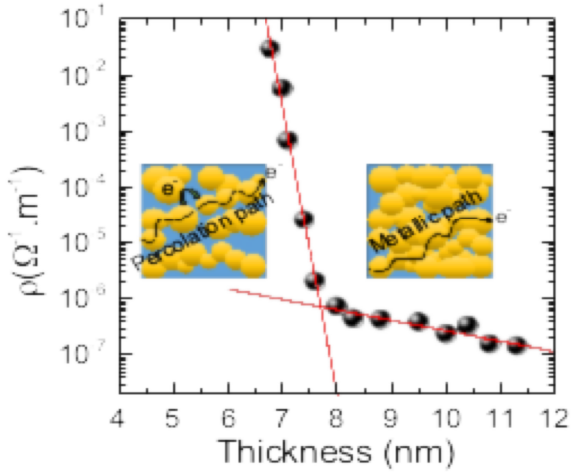

Figure 8. *Dependence of the dc resistivity of the Au NG ultrathin film on thickness. Each branch of the curve was fit to a line, and the intersection was estimated at 7.7 nm.*

For more insight into the electronic transport properties of the film, ρ_{dc} is shown in Figure 8. ρ_{dc} decreases exponentially by more than 4 orders of magnitude with an increase of 1 nm in t as a consequence of both percolation and the decrease in the tunnel barrier. There is a critical value of $t \approx 7.7$ nm estimated from the intersection of lines in Fig. 8 beyond which the NPs become interconnected yielding a continuous metallic network where ρ_{dc} is nearly constant, in good agreement with the other analyses .

Conclusions

We have investigated the optical and electrical properties along with the morphology of sputtered Au nanogranular thin film. We used an intentional deposition gradient to create nominal thickness ranging from 5 to 13 nm. The film structural characterization was performed by means of HR-TEM, AFM, XRD and XRR, where the results correlate with Volmer-Weber (VW) growth mode. The optical and electrical

measurements show a transition from dielectric-isolated gold NPs towards a continuous metallic network when *t* becomes larger than a critical value of ~7.8 nm. The onset of metallicity is clearly distinguished by the following: the bandgap of the LSPR disappear while the Drude damping factor and the plasma frequency show discontinuities as functions of thickness. All in all, the ultrathin Au nanogranular film with a linearly variable thickness described in this work could be feasible as a platform for the optimization of devices.

Acknowledgments

H. Bakkali thanks the University of Cádiz for financial support by means of (Programa de Fomento e Impulso de la actividad Investigadora 2018).

References

[1] H. Bakkali, M. Dominguez, X. Batlle, and A. Labarta, Sci. Rep. **6**, 29676 (2016).

[2] X. Batlle and A. Labarta, J. Phys. D. Appl. Phys. **35**, R15 (2002).

[3] G. Bai, C. Wu, J. Jin, and M. Yan, Sci. Rep. **6**, 24410 (2016).

[4] S. Ge, D. Yao, M. Yamaguchi, X. Yang, H. Zuo, T. Ishii, D. Zhou, and F. Li, J. Phys. D. Appl. Phys. **40**, 3660 (2007).

[5] H. Bakkali, E. Blanco, M. Domínguez, and J. S. Garitaonandia, Nanotechnology **28**, 335704 (2017).

[6] R. Sachser, F. Porrati, C. H. Schwalb, and M. Huth, Phys. Rev. Lett. **107**, 206803 (2011).

[7] M. Huth, J. Appl. Phys. **107**, 113709 (2010).

[8] H. Bakkali and M. Dominguez, EPL **104**, 17007 (2013).

[9] F. C. Motta, P. D. Shipman, and R. M. Bradley, Phys. Rev. B **90**, 85428 (2014).

[10] Y. He, J. Fu, and Y. Zhao, Front. Phys. **9**, 47 (2014).

[11] A. Barranco, A. Borras, A. R. Gonzalez-Elipe, and A. Palmero, Prog. Mater. Sci. **76**, 59 (2016).

[12] K. M. Krause, M. Thommes, and M. J. Brett, Microporous Mesoporous Mater. **143**, 166 (2011).

[13] D.-X. Ye, T. Karabacak, B. K. Lim, G.-C. Wang, and T.-M. Lu, Nanotechnology **15**, 817 (2004).

[14] H. M. Jaeger, D. B. Haviland, B. G. Orr, and A. M. Goldman, Phys. Rev. B **40**, 182 (1989).

[15] L. Ponomarenko, A. Geim, A. Zhukov, R. J.-N. Physics, and undefined 2011, Nature.Com (n.d.).

[16] K. Yoshimatsu, T. Okabe, H. Kumigashira, S. Okamoto, S. Aizaki, A. Fujimori, and M. Oshima, Phys. Rev. Lett. **104**, 147601 (2010).

[17] M. Hövel, B. Gompf, and M. Dressel, Phys. Rev. B **81**, 035402 (2010).

[18] M. Hövel, B. Gompf, and M. Dressel, Thin Solid Films **519**, 2955 (2011).

[19] H. Bakkali, E. Blanco, M. Dominguez, M. B. de la Mora, C. Sánchez-Aké, and M. Villagrán-Muniz, Appl. Surf. Sci. **405**, (2017).

[20] G. Abadias, L. Simonot, J. J. Colin, A. Michel, S. Camelio, and D. Babonneau, Appl. Phys. Lett. **107**, 183105 (2015).

[21] M. Copel, M. C. Reuter, E. Kaxiras, and R. M. Tromp, Phys. Rev. Lett. **63**, 632 (1989).

[22] R. Bhat and J. Genzer, Surf. Sci. **596**, 187 (2005).

[23] J. Siegel, O. Lyutakov, V. Rybka, Z. Kolská, and V. Švorčík, Nanoscale Res. Lett. **6**, 96 (2011).

[24] J. Laverdant, S. Buil, B. Bérini, and X. Quélin, Phys. Rev. B **77**, 165406 (2008).

[25] D. Canneson, S. Buil, X. Quélin, C. Javaux, B. Dubertret, and J.-P. Hermier, Gold Bull. **46**, 329 (2013).

[26] Y. Yagil and G. Deutscher, Thin Solid Films **152**, 465 (1987).

[27] H. Bakkali, E. Blanco, M. Amrani, J. Brigui, and M. Domínguez, Thin Solid Films **660**, (2018).

[28] M. Lončarić, J. Sancho-Parramon, and H. Zorc, Thin Solid Films **519**, 2946 (2011).

[29] A. L. Efros and B. I. Shklovskii, Phys. Status Solidi **76**, 475 (1976).

[30] Y. C. Chou and T.-S. Jaw, Solid State Commun. **67**, 753 (1988).

[31] D. Stauffer and A. Aharony, CRC Press (2014).

[32] J. Tauc, R. Grigorovici, and A. Vancu, Phys. Status Solidi **15**, 627 (1966).

[33] D. Shah, H. Reddy, N. Kinsey, V. M. Shalaev, and A. Boltasseva, Adv. Opt. Mater. **5**, 1700065 (2017).